HyperProbe

Project Title: Transforming Brain Surgery by Advancing Functional-Guided Neuronavigational Imaging

Project Acronym: HyperProbe

Grant Agreement: 101071040

Call Identifier: HORIZON-EIC-2021-PATHFINDERCHALLENGES-01

D4.1 Software tools for deep learning-based reconstruction

Leader Partner: TUM

Work Package: WP4

Author(s): Ivan Ezhov, Daniel Rueckert

Due date: Month 24

Actual delivery date date: 30.09.2024

Type: OTHER

Dissemenation level: PU

Contents

Abbreviations

- **HbO2:** Oxyhaemoglobin
- **HHb:** Deoxyhaemoglobin
- **CCO:** Cytochrome-C-Oxidase
- **redCCO:** Reduced Cytochrome-C-Oxidase
- **oxCCO:** Oxidized Cytochrome-C-Oxidase
- **HSI:** Hyperspectral Imaging
- **NIRS:** Near Infrared Spectroscopy
- **PCA:** Principal Component Analysis
- **MLP:** Multi-layer Perceptron

Disclaimer

Funded by the European Union

European Innovation Council

1 Introduction

The deliverable presents the development and testing of software tools for reconstructing morpho-chemical quantitative maps from spectroscopy imaging. The objective of the deliverable is to design algorithmic solutions that can be used to extract information about the molecular content of living tissue from spectroscopy measurements using optical systems such as the HyperProbe systems developed within the project.

The quantitative information about molecular composition can yield various biomarkers of structural and (patho-)physiological tissue properties. We aim to apply the reconstruction algorithms to monitor tissue oxygenation through the inference of endogenous chromophores, such as oxy- and deoxyhaemoglobin; to access mitochondrial metabolism and cellular energetics via cytochrome-c-oxidase; and to perform morphological tissue characterisation through a combination of molecules including also lipid and water. The algorithmic tools will be tested on datasets collected throughout the project, including ex-vivo surgical biopsies of brain tissue, in-vivo animal models, tissue phantoms, and publicly available in-vivo human studies.

Finally, the developed software will be utilized for identifying the optimal wavelength range for designing the clinical instrumentation prototypes (HyperProbe2 and 2.1).

In the following sections, we will describe several methodological approaches that we developed to address the chromophore reconstruction problem. These methods are based on deep learning as well as classical algorithms for targeted chromophore detection.

2 Identifying chromophore fingerprints of brain tumor tissue on hyperspectral imaging using principal component analysis

In the first work, we investigate the possibility of identifying the presence of chromophores in brain tissue by applying principal component analysis (PCA) to hyperspectral imaging (HSI).

HSI is an optical technique that processes the electromagnetic spectrum at a multitude of monochromatic, adjacent frequency bands. The wide-bandwidth spectral signature of a target object's reflectance allows fingerprinting its physical, biochemical, and physiological properties. HSI has been used in various applications, such as remote sensing and biological tissue analysis. Recently, HSI was also used to differentiate between healthy and pathological tissue under operative conditions in a surgery room on patients diagnosed with brain tumors.

When applied to biological tissues, HSI facilitates identifying biomarkers such as tissue metabolic activity or oxygenation. In turn, the biomarkers can shed light on the functional and pathological state of the examined tissue [21]. Differentiation between biomarkers from the reflection spectra could be achieved by relating the spectra with the absorption and scattering properties of the tissue. Absorption and scattering are the two main processes for light energy dissipation. Mathematically, one can describe their effect on the incoming electromagnetic wave via the Beer-Lambert law:

$$I_R(\lambda) = I_0(\lambda)e^{-(\mu_a(\lambda)+\mu_s(\lambda))\cdot l} \tag{1}$$

where $I_0(\lambda)$ is the intensity of the incoming light, $I_R(\lambda)$ is the intensity of the reflected light captured by the detector camera, μ_a and μ_s are the absorption and scattering coefficients, λ is the wavelength, and l is the light pathlength. The scattering process originates from different structural inhomogeneities in living tissue. The scattering coefficient μ_s is often analytically described using a low-degree polynomial dependency on the wavelength $\mu_s \sim \lambda^{(-n)}$, with n being the degree [28]. Different from the scattering, the absorption is not a bulk effect but rather occurs at the level of light interaction with single tissue molecules (or, more precisely, with molecules' chromophores). The energy dissipation due to absorption is transformed into the excitation of molecules. Since the excitation happens when light energy matches the distance between quantum energy states (which is a unique molecular property), chromophores' absorption spectra possess characteristic peaks.

Brain tissues vary in their content of chromophores. For example, blood vessels have a relatively larger concentration of hemoglobin, whereas glioma tissue presumably has a higher percentage of cytochrome (a protein actively involved in metabolic processes) [1, 55]. Thus the total absorption spectra ($\sim exp(-(\sum_i c_i \mu_a^i))$) should manifest varying spectral signatures (here c_i defines the concentration of a particular chromophore). Correspondingly, the captured reflection spectrum varies across tissue types as it is inversely proportional to the total absorption. The open question is whether one can solve the inverse problem, i.e., retrieve from the reflectance spectrum the composition of chromophores.

Several works exist attempting to perform unmixing of a reflection spectrum into a composition of chromophores spectra [11, 12]. However, the main bottleneck of recovering a physiologically complete
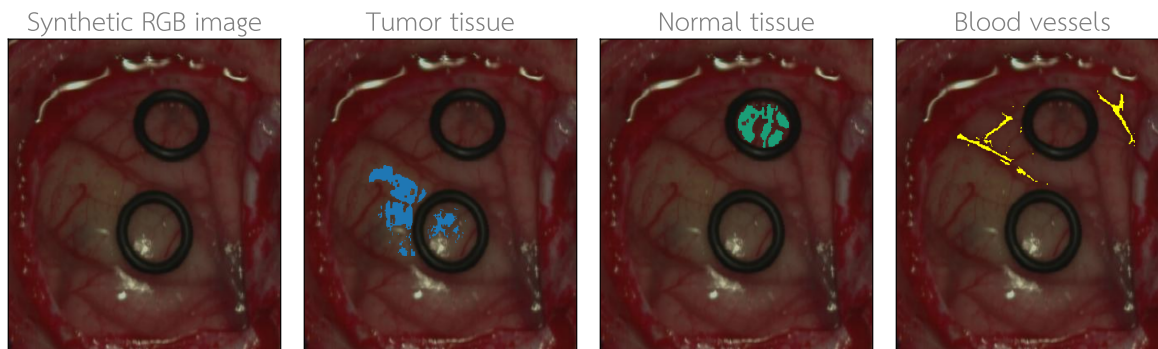
Figure 1: An example of a synthetic RGB image from the HELICoiD dataset. The image was obtained by merging three bands corresponding to red, green, and blue wavelengths from an HSI cube. The segmentations overlayed on top of the image represent three classes: tumor tissue, normal tissue, and blood vessels.
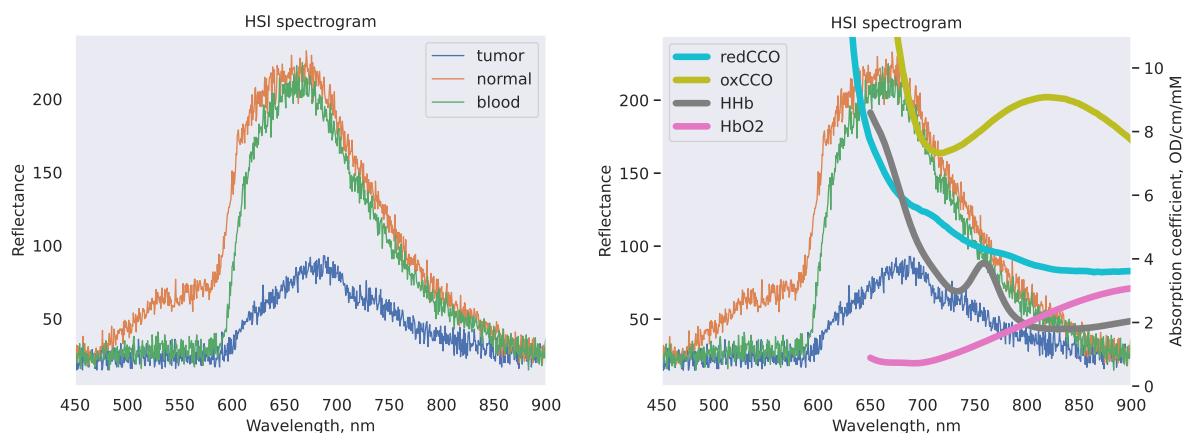
Figure 2: Raw HSI spectra for three HELICoiD classes: tumor tissue, normal tissue, and blood vessels (left). Raw HSI spectra for the three HELICoiD classes and absorption spectra of typical chromophores: reduced and oxidised cytochrome-c-oxidase, oxy- and deoxy-hemoglobin (right).

chromophore set is the ill-posedness of the inverse problem. Despite having characteristic peaks, the absorption spectra do not form an orthogonal basis within the HSI operation range of wavelengths. Thus, mathematically speaking, the mapping between reflection spectra and chromophores set is not bijective, i.e., different combinations of chromophores absorption can equally fit the reflectance. This is one of the reasons why existing works test unmixing algorithms with a limited number of chromophores in a composition.

Inspired by previous works [20, 53], we aim to identify chromophores spectra from glioma HSI images in a model-agnostic fashion by using statistical analysis means. Namely, we perform a PCA study to identify correlations between the principal components and the absorption spectra of various chromophores constituting brain tissues.

2.1 Connecting PCA with optical tissue properties

For our study, we used HSI images from the HELICoiD dataset [16]. The HELICoiD dataset consists of glioma patients which underwent HSI monitoring during surgical operations. The image dimensions are of varying spatial size across the dataset but with a fixed spectral size of 826 bands. The images were sparsely labeled (less than 25% of the image area) into four classes: tumor tissue, normal healthy tissue, blood vessels, and background, Figure 1. We preselected twelve patients which were diagnosed with grade IV glioblastoma as the primary tumor. From each of the preselected patients, we extracted spectra that belong to three classes (all HELICoiD classes, except the background). In total, we collected 30k spectra equally distributed over the three semantic classes. Figure 2 demonstrates typical raw spectral profiles for each class. The absorption spectra were taken from the BORL GitHub repository [47].

Next, we performed the PCA for all 30k spectra in a high-dimensional space ($\mathbb{R}^{826}$) to identify axes of the highest variance. Our reasoning here is that, on one side, the projections of the first principal

component (or a few first ones) into the original basis would inform us on how each HSI spectral band is important for capturing the data variance. On the other hand, the spectral variance between the tissue classes originates from the different distributions of chromophores' concentrations. Therefore, we expect to observe a correlation between the principal components and the absorption spectra of chromophores.

We performed PCA in two different settings:

1. First, we wanted to identify the principal components for a mixed dataset composed of spectra from different tissue classes. Such a test would allow determining spectral bands that best differentiate between the classes. Figures 3 and 4 show the results of such PCA tests. Here, ntb denotes the 1st principal component for a dataset composed of all three classes, nt - for normal and tumor tissue samples, nb - for normal tissue and blood vessels. We visualize only the 1st component weights since it explains more than 98% percent of the variance.
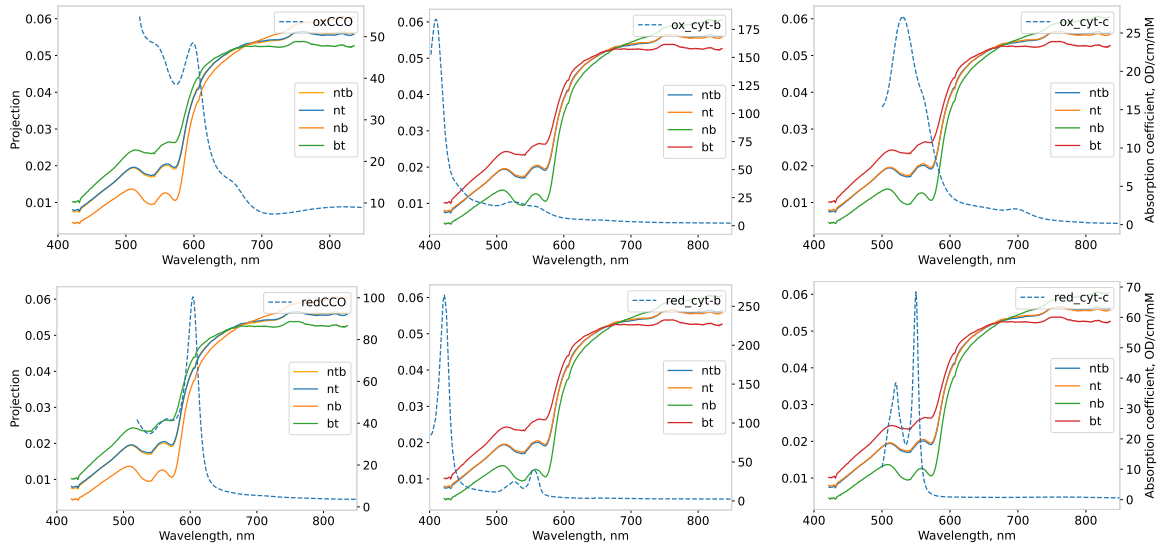
Figure 3: Absorption spectra of cytochromes: oxidized (upper row) and reduced (bottom row) of three prosthetic group types (CCO, cyt-b, and cyt-c). In solid line, we show the 1st principal component for four different datasets: "ntb" denotes a dataset composed of all three classes (normal tissue, tumor, blood vessels), "nt" - is for normal and tumor tissue samples, "nb" - for normal tissue and blood vessels, and "bt" - for blood vessels and tumor. Reduced cytochrome-c-oxidase (redCCO) reveals the highest correlation with the principal component.

As evident from the figures, the range between 500 and 600 nm brings the highest correlation. Particularly absorption profile of the reduced cytochrome-c-oxidase (redCCO) reveals a very close match with the principal component. This can confirm our original hypothesis, as this is the interval of wavelengths where redCCO has characteristic absorption peaks. Cytochromes are present in a high concentration in the tumor microenvironment, less so in normal tissue, and only marginally in the endothelial cells of the inner walls of blood vessels. Our statistical analysis accurately captures this biological fact - the 1st principal component has the highest weights for separation between tumor tissue and blood vessels (bt) while having smaller weights for tumor against normal tissue (nt) and the blood versus normal tissue (nb) separation.

2. We wanted to test whether PCA can reveal spectral signatures correlated with molecular absorption within a single class. This test is motivated by the fact that glioma tissue possesses high variability of cytochrome concentration since the tumor is vastly heterogeneous. In enhancing actively proliferating tumor, the hypermetabolism should be accompanied by an abnormal cytochrome amount [1]. In contrast, no proliferation is expected in the necrotic core area, and thus, the concentration of cytochrome should be minimal. Therefore the weights of the 1st principal component are expected to be aligned with the cytochrome absorption and be more pronounced for the tumor class than for healthy tissue and vessels. This was also confirmed by the PCA, as seen in Figure 5 - the 1st principal component of the dataset composed of tumor samples has the highest weight in the 500-600 nm range. We want to point out that total absorption from any tissue class is a combination of absorption from a set of chromophores. For example, Figure 4 illustrates that oxy- and deoxyhemoglobin also have characteristic peaks in this interval. Hemoglobin concentration in tissues, though, has a contrary distribution to cytochrome, being higher in blood vessels and less in tumor and normal tissues. However, as discussed just above, the intra-class PCA rather captures the relation between tissues in its dependency on cytochrome. This poses the question
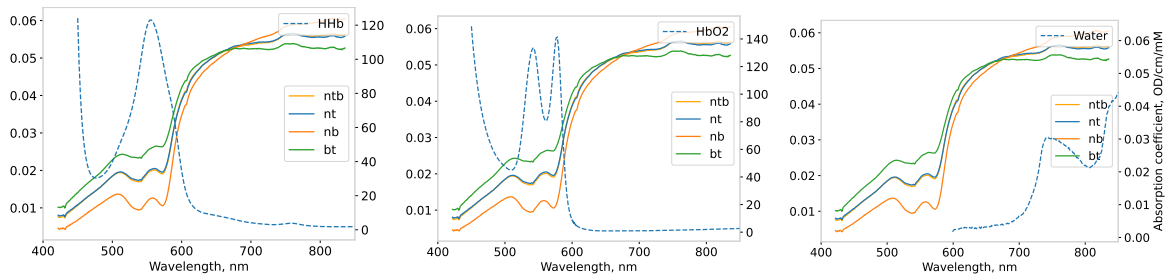
Figure 4: Absorption spectra of hemoglobin, deoxy- (left) and oxy- (middle), and water(right). In solid line, we show the 1st principal component for four different datasets: "ntb" denotes a dataset composed of all three classes (normal tissue, tumor, blood vessels), "nt" - is for normal and tumor tissue samples, "nb" - for normal tissue and blood vessels, and "bt" - for blood vessels and tumor.
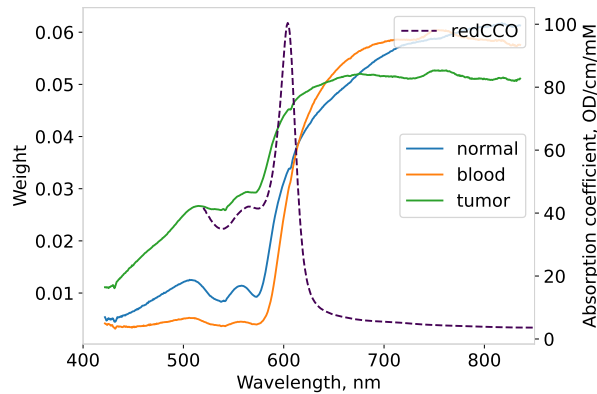
Figure 5: Absorption spectra of reduced cytochrome and PCA components. In solid line, we show the 1st principal component for four different datasets: "ntb" denotes a dataset composed of all three classes (normal tissue, tumor, blood vessels), "nt" - is for normal and tumor tissue samples, "nb" - for normal tissue and blood vessels, and "bt" - for blood vessels and tumor.

of whether the observation is due to a much higher concentration of cytochrome than hemoglobin in tissues or a much larger variance in cytochrome within a tissue class. We did not find evidence for the former in literature, rather opposite is typically observed [24]. And if the latter is true, the difference between the magnitude of the principal components for the three tissue classes can quantify the intra-class chromophore variance. Such knowledge helps in understanding plausible ranges of concentration which is in turn valuable for deciphering the molecular profiling of tissue.

To conclude, in this work, we analyze HSI glioma images from the HELICoiD project. We perform a PCA-based statistical analysis of this dataset to identify chromophore absorption signatures in the HSI reflection spectra. PCA revealed the correlation of chromophores, especially cytochrome, with the principal components. We discuss the possibility of using such analysis to decypher relative chromophore concentration in brain tissues. We see such analysis as a vital tool for the identification of chromophore fingerprints complementing traditional spectral unmixing techniques.

3 Learnable real-time inference of molecular composition from diffuse spectroscopy of brain tissue

In our next work, we developed a data-driven technique for inferring molecular composition changes from diffuse spectroscopy of brain tissue, enabling real-time intra-operative monitoring. Our motivation stems from the fact that no established method exists to streamline the inference of the biochemical composition from the optical spectrum for real-time applications. However, various biomedical applications, such as neurosurgery, have an unmet need for rapid monitoring of intrinsic tissue properties [18, 19, 39]. Spatially-resolved maps of the tissue characteristics would allow bypassing invasive disease diagnostics, e.g., biopsy, which halt the operation. Instead, a surgical decision could be made during the operation, reducing its time and preserving a healthy brain.

As mentioned in the first section of the deliverable, analytical and statistical approaches exist aiming to unmix optical spectra into the physical phenomena defining the spectra profile under a limited data

regime [6, 11, 15, 20, 34, 48, 53]. A large number of methods mitigate the data scarcity by introducing a physical prior to establish the spectrochemical link. Typically, the modified Beer-Lambert law [40, 46] is used to provide such a link by describing the incoming light's energy dissipation as an exponentially decaying function:

$$\log(I_R(\lambda)/I_0(\lambda)) = - \left[\sum_i c_i \mu_a^i(\lambda) + s\mu_s(\lambda) \right] l + U \tag{2}$$

Here, $I_R(\lambda)$ and $I_0(\lambda)$ are the intensities of the reflected and the incoming light, μ_a and μ_s are the absorption and scattering coefficients, the index i denotes the molecule constituting the tissue such as water, fat, hemoglobin and cytochromes, c_i denotes the corresponding concentration (e.g. as volume fraction), and s is the weight of scattering in the total light energy dissipation. The remaining quantities are λ, which is the light wavelength, l is the light pathlength*, and U describes other physical factors contributing to the energy dissipation of the incoming light or other sources of the optical signal captured by the light detectors or cameras.

Typical molecules whose changes in concentration are inferred include oxyhemoglobin, deoxyhemoglobin, and cytochrome-c-oxidase (CCO) [22]. Measurement of the former two chromophores can reveal e.g. oxygenation status of the brain, and can help determine hypoxic or hyperoxic conditions. CCO is a fundamental metabolic molecule correlated to ATP production during cellular respiration, which has previously complemented obtained hemodynamic information in various applications [4, 22].

Now, in the case of changes in molecular composition over the course of optical monitoring, one can assume that the effects contributing to U either stay constant (e.g., which is a fair assumption for ambient illumination) or change notably less than the total absorption†. Under this assumption, subtraction of two reflection spectra, $\log I_R^2 - \log I_R^1$ (traditionally, these have been two different points in time, but this could also be true for different points in space), would cancel out or make negligible the term $\delta U = U^2 - U^1$ in the following equation:

$$\log(I_R^2(\lambda)/I_R^1(\lambda)) = - \left[\sum_i \delta c_i \mu_a^i(\lambda) + \delta(s\mu_s(\lambda)) \right] l + \delta U \tag{3}$$

In such a differential form, the modified Beer-Lambert law can now be used to identify molecular composition. For this, standard least-squares optimization algorithms (or non-negative matrix factorization [8, 34]) can be employed to minimize the difference between the real spectra and the spectra obtained from the modified Beer-Lambert law. As a result of the minimization, the optimal values of the set of concentration changes $\{\delta c_i = c_i^2 - c_i^1\}$ are obtained (alongside the scattering parameters).

The overarching drawback of this approach is the computational time it takes to infer the biochemical composition. For example, the optimization methods take a subsecond time to infer the composition of a single spectrum containing a number of wavelengths typical for bNIRS and HSI (a few hundred). However, for real-time applications particularly in the case of HSI modality, one needs to solve the optimization task in a subsecond time for as many spectra as there are spatial pixels, as every pixel contains its own spectrum. The number of pixels on a hyperspectral image can be easily in the order of 10^5-10^6. Providing subsecond timings for simultaneous inference on such an amount of spectra poses a challenge for traditional methods.

Contributions. There are numerous studies analyzing the application of machine learning methods to achieve fast inversion of the physical models based on Beer-Lambert law or Monte-Carlo simulations [9, 17, 27, 37, 41, 45, 51]. Predominantly they imply training a machine learning model on synthetic data generated by following the chosen physical formalism, and then evaluating the trained model on real spectra. While proven to work for the use cases mentioned in the cited works, this approach might be inferior as synthetic data generators likely underestimate the complexity of real data. To mitigate this, we tested different strategies for model training using only the *synthetic data* as in previous works or incorporating *real data* via traditional optimization in the training procedure.

Second, we test the proposed method on its ability to approximate physical models of varying complexity: *linear* (absorption only) and *non-linear* (absorption combined with scattering). While evaluated independently in previous works, here we also analyse our approach to explicitly compare both

---

*Even though several works demonstrate the importance of wavelength-dependent definition of the pathlength [3], in what follows, for simplicity, we opted for constant pathlength independent of the wavelength.

†In certain scenarios, even changes in scattering are not expected since it is a rather bulk effect dependent on the density of the probed matter rather than molecule-specific one.

models in terms of spectral fit. This comparison is motivated by a desire to elucidate the conditions under which the linear model (that can be easily solved using, e.g. pseudoinverse) is appropriate for describing the light-brain matter interaction process, and where inclusion of the scattering is necessary.

Third, given that the work is carried out within the HyperProbe project [25] aiming to achieve real-time brain tissue monitoring, the present paper evaluates the *computational timing* for the biochemical composition inference across different methods and hardware platforms. To reinforce the comparison, in contrast to previous works manually choosing the hyperparameters' values of the machine learning methods, we used the AutoML technique [32] to identify the most optimal hyperparameters set.

Finally, to our knowledge, this is the first work that applies a neural-network-based approach to provide real-time inference of chromophore composition from *in-vivo brain tissue* spectroscopy measurements [2, 7, 10, 13, 29, 36, 43, 52, 54]. We evaluate and discuss applicability of the method on broadband NIRS (transmission mode) [30] and hyperspectral (reflection mode) [16] measurements of brain tissue.

As mentioned in the introduction, inference of absolute chromophore concentrations from an optical spectrum is a challenging task due to multiple physical effects shaping the reflection spectrum. Thus, we instead aim to predict the changes in concentrations from changes in the spectra, Eq. 3.

Generating a dataset	Training a network	Inference
We generate a dataset of optical spectra - molecular concentrations pairs using the modified Beer-Lambert law and traditional least squares minimisation	We train a neural network on the generated data to learn a mapping between the spectral and concentrations change	Finally, we use the trained network to predict the concentrations change from reflection spectra in the test set

$$\log\left(\frac{I_R^2(\lambda)}{I_R^1(\lambda)}\right) = -\left[\sum_i \delta c_i \mu_a^i(\lambda) + \delta\left(s\mu_s(\lambda)\right)\right] l$$

Figure 6: The general pipeline describing the learnable approach for inferring concentrations' changes of molecules such as reduced and oxidized cytochrome-c-oxidase, oxy- and deoxy-hemoglobin $\{\delta c_i\} = \{\delta redCCO, \delta oxCCO, \delta HHb, \delta HbO_2, etc\}$. The pipeline involves training on a dataset which is generated by the means of a modified Beer-Lambert model. According to the model, the light reflection I_R is shaped by the absorption μ_a and scattering μ_s phenomena.

3.1 Datasets creation

In our method, Fig. 1, we use a supervised data-driven approach by creating a dataset of attenuation-concentration pairs to train a neural network (by attenuation, or more precisely the change of it, we imply the logarithm of the reflection: $\Delta A = \log I_R^2 - \log I_R^1$). We employ two different strategies to create the dataset:

a) The first strategy directly utilizes the modified Beer-Lambert law to generate the training dataset pairs $(\Delta A, \{\delta c_i\})$ with ΔA being the difference in attenuation between two spectra and $\{\delta c_i\}$ the corresponding differences in concentration of chromophores, Fig. 2 (a). For each chromophore, we randomly sample values for changes in the molecular composition $\{\delta c_i\}$ using the uniform distribution within physiologically plausible ranges. These ranges were determined based on values typically used in the literature, and further details are provided in the appendix.

If scattering is included in Eq. 3, we may assume it to be of rational form:

$$s\mu_s(\lambda) = s\left(\frac{\lambda}{500nm}\right)^{-b} \tag{4}$$

with the scaling of the anisotropy $g = 0.9$ included in $s = s'/(1 - g)$ [22, 28]. In the differential form, we
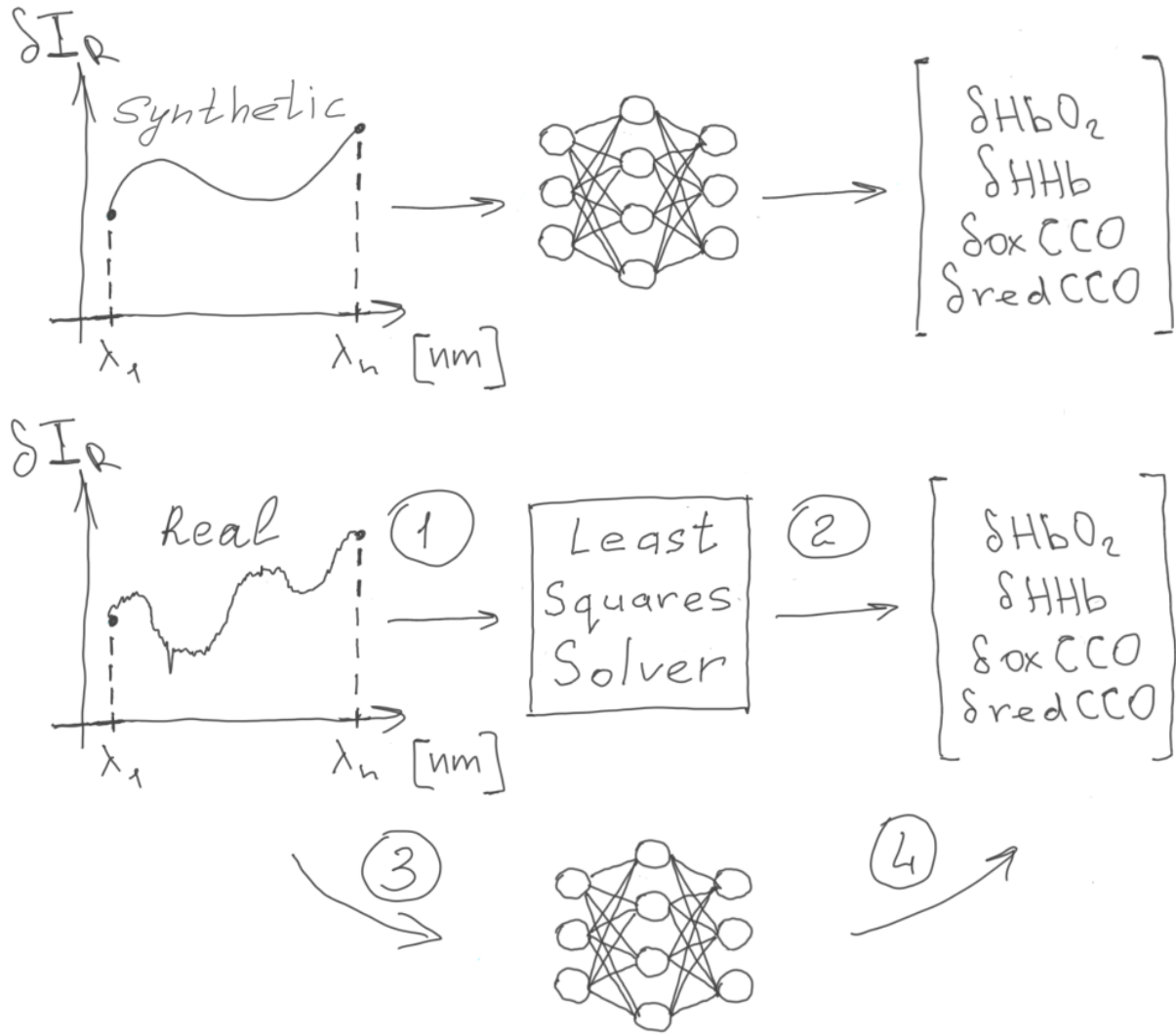
Figure 7: Two strategies for collecting the training dataset. Strategy (a) in which we train a network on synthetic attenuation-concentration pairs generated from the modified Beer-Lambert law, above. Strategy (b) in which the training is performed on pairs of real attenuation and concentrations obtained through the least-squares fit to the corresponding real spectra, below.

obtain

$$\delta(s\mu_s(\lambda)) = s_2 \left(\frac{\lambda}{500nm}\right)^{-b_2} - s_1 \left(\frac{\lambda}{500nm}\right)^{-b_1} \tag{5}$$

and therefore also uniformly sample parameters s_1, s_2, b_1, b_2 within plausible ranges [28]. Subsequently, we input the obtained values into the modified Beer-Lambert law to obtain synthetic differential attenuations $\Delta A(\lambda)$. This difference in attenuation ΔA as input and the corresponding $\{\delta c_i\}$ as output are then used for training.

b) Given that the distribution of the synthetic spectra obtained according to the strategy described above can be notably different from the distribution of real spectra, this can result in an unsatisfactory network prediction accuracy. Therefore, in addition to (a), we evaluate another strategy for creating a dataset trying to bridge the gap between the physical model and real data, Fig. 2 (b). For this, we use traditional least squares minimization to fit the changes in the real reflectance spectrum with the modified Beer-Lambert law. The concentrations $\{\delta c_i\}$ found upon the optimization and the corresponding ΔA constitute the training samples.

3.2 Network and optimization details

The training was performed using a multi-layer perceptron (MLP [44]) neural network for both approaches. The network takes as input a one-dimensional vector of attenuation difference and outputs molecular concentration changes.

We trained both networks with early stopping when they reached convergence. To find the optimal network architecture, we used the Ray Tune library [32] to validate different MLP architectures (width, number of hidden layers, and activation functions), learning rates, and batch sizes. More details regarding the networks and the training procedure can be found in the appendix.

Least squares optimization for the Beer-Lambert law, excluding the scattering effect, can be performed via multiplication of the observed attenuation with the pseudoinverse of the absorption coefficients [22]. In order to perform the nonlinear least-squared optimization for the Beer-Lambert law model including scattering, we used the publicly available solver of the SciPy library [50]. We used the least-squares minimization obtained predictions as the ground truth to validate all the trained networks.

3.3   Data

For our experiments, we applied two types of Beer-Lambert law formulation, with and without scattering, to two types of spectral datasets: broadband NIRS data for which the spectra were measured in light transmission mode [30] and hyperspectral data which were obtained in non-contact reflection mode [16].

3.3.1   Broadband NIRS

The first dataset is composed of broadband NIRS spectra from a study analyzing 27 piglets' brains in which a hypoxia-ischemia (HI) state was induced [30]. The piglets were monitored for several hours, during which the carotid arteries were surgically isolated, and a stepwise hypoxia took place for 15-20min. This produced a significant hypoxic-ischaemic effect that changed the metabolic status of the brain and, in some instances, caused further brain injury. The details of the intervention protocol are described in [30]. The optical device used in the study utilizes a miniature light source and a customized high-throughput miniature spectrometer, connected to high numerical aperture optical fibers. The measurements contain around eight thousand spectra per piglet. The distance between each measured time point is between 10.0 and 10.5 seconds. We use the first thousand measurements, i.e. we only consider the first ∼2.5 hours of measurement. For all piglets, this is sufficient to observe HI and recovery after HI. As Eq. 3 requires defining a baseline spectrum, analogously to [30], we used a spectrum at the very beginning of optical monitoring (i.e., before HI) for the baseline. We normalized the spectra with respect to dark noise and white reference. The normalized bNIRS spectra before and after the intervention inducing hypoxia are shown in Fig. 8 (left), and predictions of the concentrations change over the course of the optical monitoring are shown in Fig. 8 (right). Out of the 27 piglets in the dataset, 25 had data available during HI, such that 19 were used for training, two for validation, and four for testing. For this dataset, we predict three types of molecules: oxyhemoglobin, deoxyhemoglobin, and differential cytochrome-c-oxidase
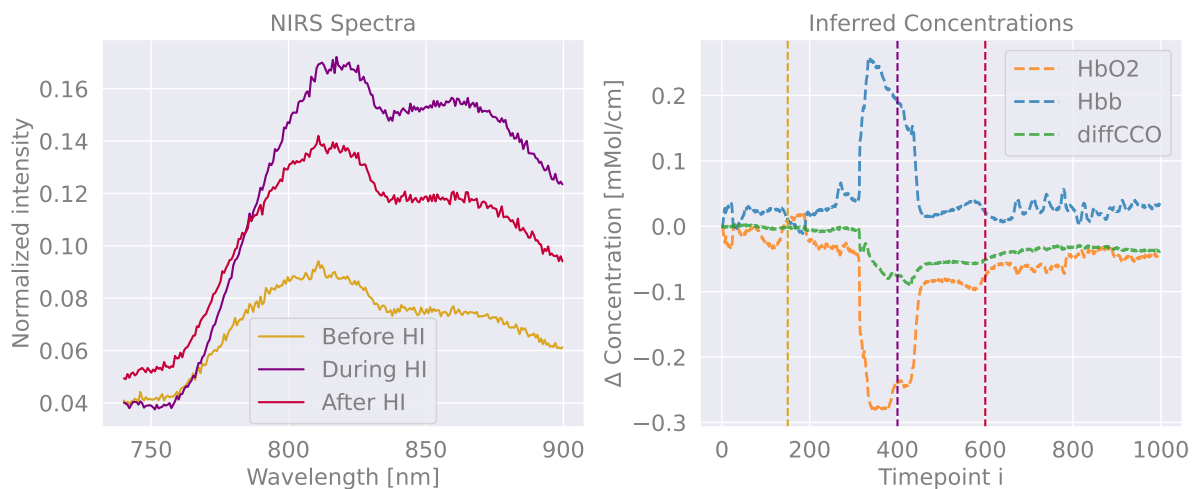
Figure 8: Optical spectra from the broadband bNIRS study in [30] before, during and after inducing HI in the piglet's brain (left). On the right, predictions of the molecular concentration change $\{\delta c_{HbO_2}, \delta c_{HHb}, \delta c_{\text{diffCCO}}\}$ over the course of the optical monitoring (for the Beer-Lamber model *without* scattering). The vertical lines denote the time points corresponding to the normalized reflection spectra on the left.
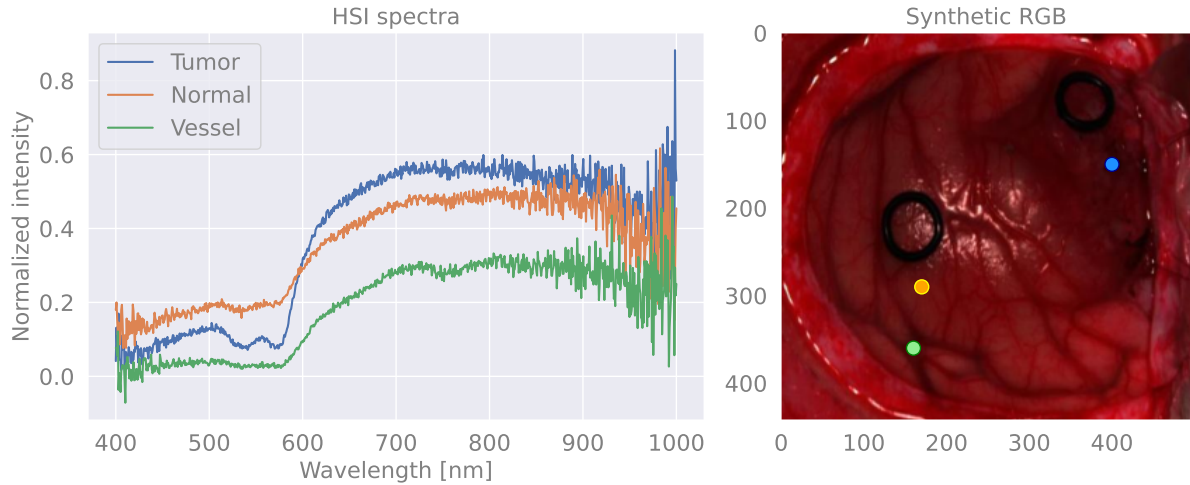
Figure 9: Optical spectra from the HSI study of patients diagnosed with glioma [16] for different tissue types: tumor, normal tissue, and blood vessels (left). On the right is a typical RGB image of the brain surface, which is obtained from the HSI volume. The dots correspond to the spectra on the left image. The black circles on the RGB image are rubber rings that surgeons used to mark tumomr and healthy tissues.

(CCO)†, i.e. $\{\delta c_i\} = \{\delta c_{HbO_2}, \delta c_{HHb}, \delta c_{\text{diffCCO}}\}$, where $\delta c_{\text{diffCCO}} = \delta c_{oxCCO} - \delta c_{redCCO}$. We neglected the potential contribution to the spectra from water and fat due to their minimal change in concentrations during the 2.5 hours of monitoring [24, 30]. Note that we assume unitary pathlength in our experiments, which results in units of [mM/cm] and [1/cm] for the inferred concentrations. In the NIR range, it has been shown that the pathlength is semi-constant [30], which effectively leads to a simple rescaling in our concentrations when using this assumption. This can also be observed when comparing the inferred exemplary concentrations from Fig. 8 (right) with pathlength-corrected concentrations in previous work [30].

3.3.2 Hyperspectral data

The second dataset we used consists of hyperspectral data from the Helicoid project [16]. The Helicoid dataset comprises brain HSI images obtained in surgical conditions from 22 patients diagnosed with glioma. The optical instrumentation is based on pushbroom technique and a silicon CCD detector array as a camera. The HSI images provide a high spectral resolution of 826 bands spread between 400 and 1000 nm and a 2D spatial resolution of a few hundred pixels in each dimension. The images were also expert-annotated into three tissue classes: normal and tumor tissues, as well as blood vessels. Typical hyperspectral image and corresponding spectra are shown in Fig. 9. Different from the bNIRS dataset, we used a spectrum of the pixel belonging to the blood vessel class as a baseline spectrum§. We then subtracted the baseline spectrum from all other spectra in the same image. In other words, we performed the differential spectroscopy *not in time but in space*.

Besides predicting oxyhemoglobin δc_{HbO_2} and deoxyhemoglobin δc_{HHb}, we again infer the differential cytochrome-c-oxidase concentration due to its role in capturing oxidative metabolic activity. We separately predicted oxidized cytochrome-c-oxidase and reduced cytochrome-c-oxidase, as the total CCO concentration may not be assumed to remain constant in space. We also predict water and fat since, for these molecules, one cannot assume minimal concentration change across different tissue types as in the case of the bNIRS spectra. For reference, the absorption spectra can be found in the appendix.

Fig. 10 showcases examples of molecular inference for the HSI images from the Helicoid dataset. Out of the nine patients with glioblastoma in the dataset, six with distinct class labeling were chosen,

---

†As the total CCO concentration may be assumed to not change within a few hours, the oxidized-reduced difference spectrum μ_a^{diffCCO} may be used to infer changes of both oxidized and reduced CCO [4].

§The blood vessel was used as a reference for a couple of reasons. The blood vessel is clearly distinguishable from the other two tissue types, tumor and non-tumor tissue. These two types of tissue are highly heterogeneous, e.g. within a pixel area, they can have small capillaries, leakage of blood, agglomeration of dead cells, etc. In contrast, the blood vessel pixels, especially the ones belonging to large arteries, are less heterogeneous. Moreover, it is assumed that blood vessels do not possess cytochrome molecules. Thus, it is a better reference when one sets a goal of detecting the presence of cytochromes in the brain matter.
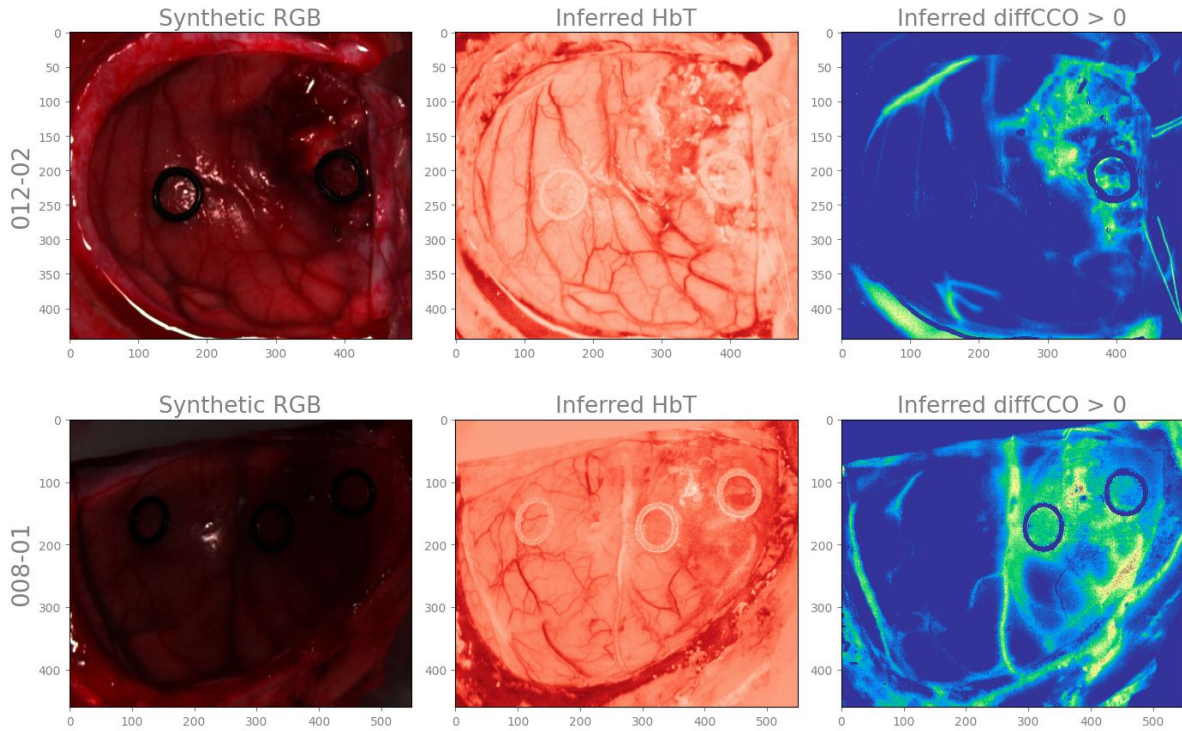
Figure 10: Examples of HSI images of two patients, shown with respective patient ID, from the Helicoid dataset [16] (left). Each pixel in the shown 2D image possesses a spectral signature with 826 bands. From this signature, we predict the molecular concentration change for hemodynamic $\delta c_{HbT} = \delta c_{HbO_2} + \delta c_{HHb}$ (middle), and metabolic $\delta c_{\text{diffCCO}} = \delta c_{oxCCO} - \delta c_{redCCO}$ characterization (right). Here, we use the Beer-Lambert model *with* scattering, as it provides a closer fit to real spectra than the model without scattering. We observe that performing the spectral unmixing on the HSI measurement of brain tissue allows us to better contrast the vessel tree (middle) and tumor area (right) than on the RGB image.

and three patients were used for training, one for validation, and two for testing. Note that patients might have multiple images taken, and different images from the same patient were assigned to the same training, validation, and test set to avoid set contamination. Therefore, the training set consists of five, the validation set of one, and the test set of three images.

3.4   Scattering vs Non-scattering

First, before discussing the learnable methods for molecular inference, we test different Beer-Lambert law formulations - with and without scattering - to elucidate limits of applicability of both models. For the case of piglets undergoing HI, it is widely assumed that the 780nm to 900nm range is predominantly dominated by absorption, with scattering being only a minor contributor to the overall measured spectrum [30]. As measurements in the piglet dataset below the 780nm threshold were available, we opted to extend the model fitting range from 740nm to 900nm. This test is motivated by our desire to assess whether a linear model (without scattering) would still be sufficient to describe the broader spectroscopy measurement of brain tissue.

Fig. 11 shows spectral fits using both formulations. The model with scattering provides a clearly better fit. It allows us to better describe the peak around 760 nm for the bNIRS data, while for the HSI data, the inclusion of scattering is often merely necessary for an accurate fit of the spectra in this wavelength range. This finding is consistent across the dataset, as shown in table 1.

To show that the model with scattering can significantly improve model fits, especially for the higher frequency portion of the spectrum, we evaluate the relative improvement r in terms of the spectral fit of the scattering model compared to the non-scattering model. We use mean absolute error (MAE) as a measure of the fit and compute it for all piglets across different spectrum bands.

The spectral fit MAE is calculated by

$$\text{MAE} = \frac{\sum_{i=1}^{n} |\Delta A_{model}(\lambda_i) - \Delta A_{data}(\lambda_i)|}{n} \tag{6}$$

where $\Delta A_{model}(\lambda_i)$ represents the model-inferred attenuation at wavelength λ_i, and ΔA_{data} the real
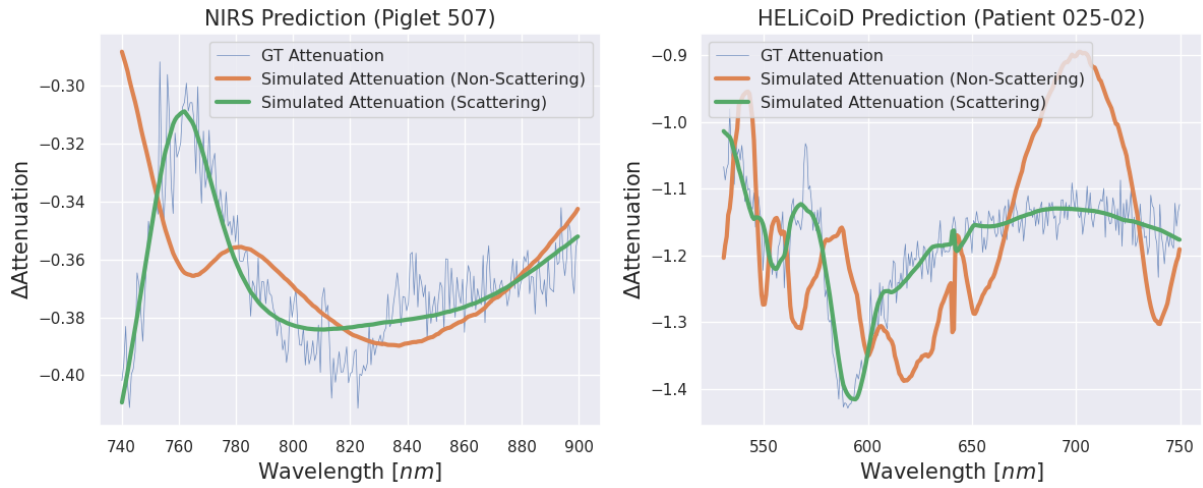
Figure 11: Comparison between predictions using linear (no scattering) and non-linear (with scattering) models for bNIRS (left) and HSI (right) spectra. The ground truth (GT) attenuation is computed from the real spectra difference. The inclusion of scattering into the formulation of the Beer-Lambert law notably improves the spectral fit to real data.
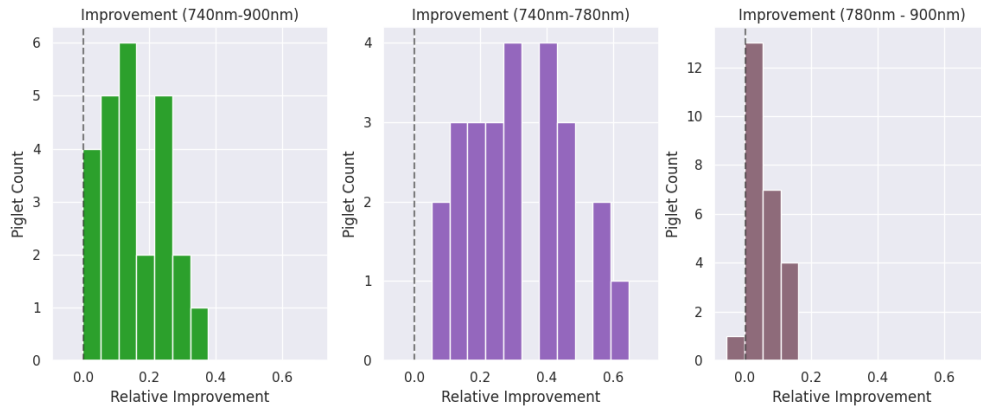
Figure 12: Histograms showing mean relative improvement of the spectral fit MAE for presented scattering model, compared to the linear model, across all piglets in the dataset for all wavelengths (left), in the range 740nm-780nm (middle), and in the range 780nm-900nm (right) in the broadband NIRS dataset. The x-axis represents the relative improvement r between the two models, and the y-axis shows the number of piglets that achieved the corresponding mean relative improvement r. The dashed line signifies improvements below zero, i.e. cases where the spectral fit worsened.

measured attenuation, respectively. The relative mean improvement is computed by

$$r = \frac{\text{MAE}_{scatter} - \text{MAE}_{linear}}{\text{MAE}_{linear}}$$

comparing the improvement in mean error between the scattering and linear models, computed across all timepoints.

The results of such computation for all piglets are shown in figure 12, where we observed a mean relative improvement of 15.7% over the full fitting range. Such improvement is especially noticeable in the 740nm to 780nm range, where the mean improvement of the distribution almost doubled at 30.8%. The spectral fit does not improve significantly in the 780nm to 900nm range, with the mean relative improvement of the distribution being at merely 5.6%. For one of the 25 piglets, we observed that the spectral fit slightly worsened in the 780nm to 900nm range through the nonlinear model. However, the fitting MAE is only worse by 0.6%, and the spectral fit was still better for the overall range and in the 740nm-780nm range. We therefore can still confidently conclude that the presented model is able to fit the piglets' measured spectra more closely, especially for presumed scattering-dominated bands.

The necessity of the scattering consideration in the Beer-Lambert model for the HSI data can be explained by the more pronounced contribution of the scattering process. For the HSI data, we infer the

difference in molecular composition between different spatial locations on an image, i.e., between different tissue types. The scattering property across brain tissues can significantly vary, and thus, the scattering shapes markedly the differential spectra. In contrast, for the bNIRS data, we perform the differential spectroscopy analysis not in space but in time (comparing two spectra for the same location taken at different time points), meaning that the molecular inference is performed for the same tissue type.

In conclusion, we find that the non-linear model is especially helpful in describing scattering-dominated bands. However, the linear model may still be used when absorption is the prevalent physical effect.
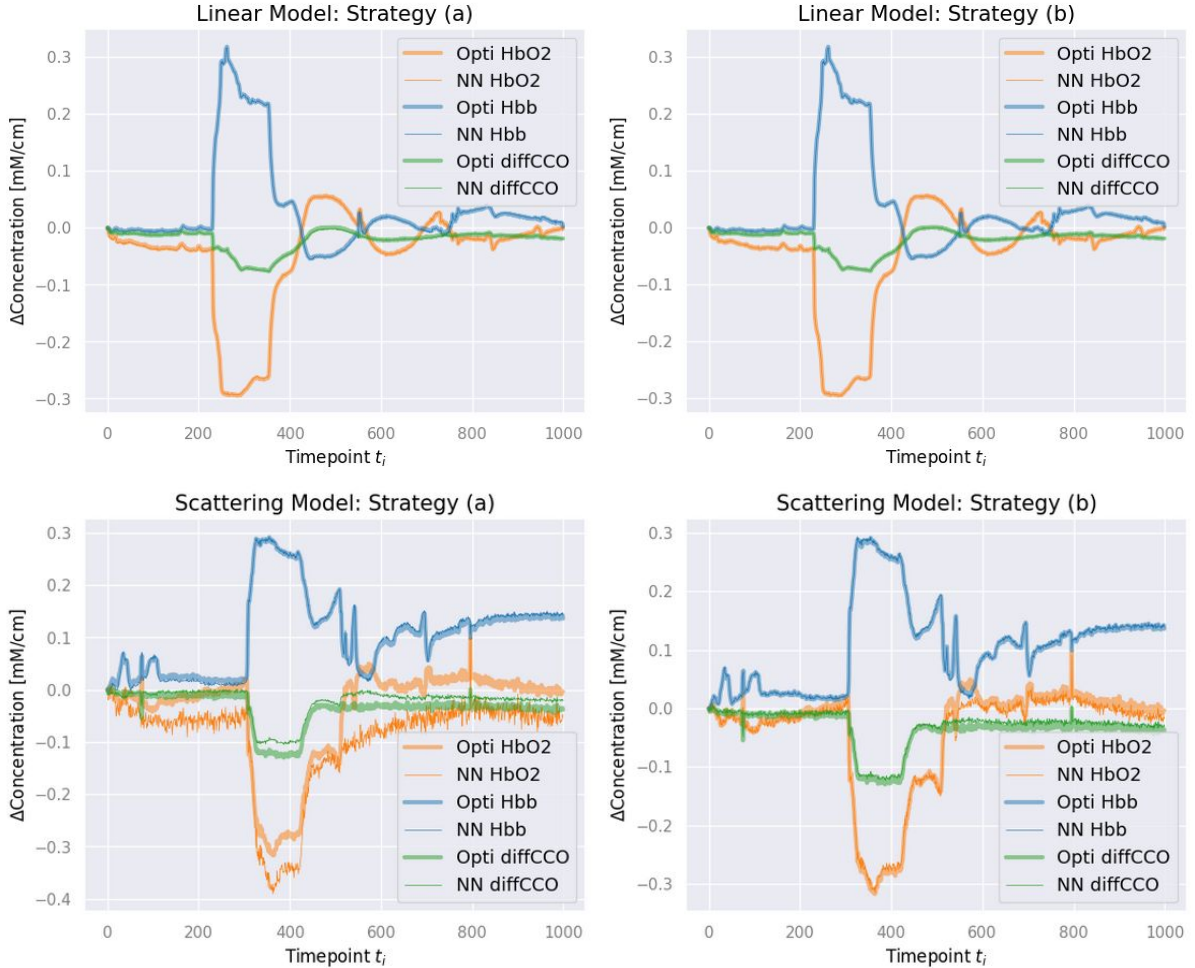
Figure 13: Comparison between inference of the molecular composition using the standard optimization methods and proposed network-based inference for training strategy (a) and (b) on the bNIRS dataset. The top row compares both strategies when using the linear model, where highly accurate neural network predictions are visible in both cases. The bottom row compares the strategies when using the non-linear model, with strategy (b) delivering noticeably more accurate predictions.

3.5 Evaluating different training strategies

Next, we evaluate the proposed machine learning approach in its ability to substitute both the linear absorption and the non-linear scattering model.

Fig. 13 demonstrates the results of the experiment in which we test the network trained on synthetic data collected according to strategy (a) and on real data according to strategy (b), for both linear and non-linear models. For the linear case, both strategies are able to correctly infer the concentrations. The solution to the linear model can merely be found by a matrix multiplication, i.e. the pseudoinverse, which is why both strategies are able to very accurately predict the optimization-inferred concentrations.

For the non-linear case, strategy (b) provides qualitatively closer fits. We also tested this model for the Helicoid dataset, where we found highly matching results by the use of strategy (b), as seen in Table 1.

Dataset	Individual ID	Spectral MAE		Concentration MAE	
		Non-Scattering	Scattering	Strategy (a)	Strategy (b)
Broadband NIRS	507	1.23×10^{-2}	$\mathbf{8.60 \times 10^{-3}}$	1.36×10^{-2}	$\mathbf{4.32 \times 10^{-3}}$
	509	1.09×10^{-2}	$\mathbf{9.37 \times 10^{-3}}$	2.46×10^{-2}	$\mathbf{4.81 \times 10^{-3}}$
	511	8.01×10^{-3}	$\mathbf{6.60 \times 10^{-3}}$	1.16×10^{-2}	$\mathbf{3.41 \times 10^{-3}}$
	512	1.20×10^{-2}	$\mathbf{1.09 \times 10^{-2}}$	1.25×10^{-2}	$\mathbf{4.59 \times 10^{-3}}$
HELICoiD	012-01	3.27×10^{-2}	$\mathbf{2.49 \times 10^{-2}}$	1.73×10^{-1}	$\mathbf{1.64 \times 10^{-2}}$
	012-02	2.24×10^{-2}	$\mathbf{2.19 \times 10^{-2}}$	1.50×10^{-1}	$\mathbf{2.58 \times 10^{-2}}$
	015-01	6.33×10^{-2}	$\mathbf{2.54 \times 10^{-2}}$	1.75×10^{-1}	$\mathbf{1.54 \times 10^{-2}}$

Table 1: Quantitative performance comparison of the different Beer-Lambert models and network training strategies on the test set of the two spectral datasets. To compare the two (non-scattering and scattering) models, we compute the mean absolute error of the spectral fit (denoted as 'Spectral MAE') between the ground truth observed and predicted signals. The two network training strategies are compared by assessing the mean absolute error of each strategy between the network and optimization-inferred concentrations (denoted as 'Concentration MAE') of all considered chromophores. In the case of the HELICoiD dataset, only pixels labeled as normal, tumor, or blood were considered for these computations. The best-performing model and strategy for each individual is highlighted in bold.
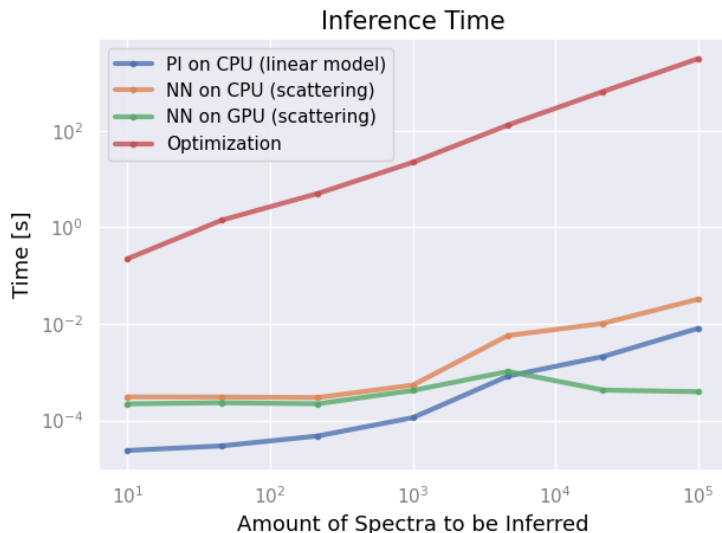
Figure 14: Comparison between inference time for various optimization approaches for varying number of spectra (from 10 to 10^5): including the pseudoinverse for the linear model (blue) and optimization-based (red) for the non-linear scattering model (both running on CPU), as well as network-based approach for scattering model running on CPU (orange) and GPU (green).

3.6 Computational time

Importantly, the proposed network-based optimization comes with a significant speed-up in computational time. In Fig. 14, we show a comparative analysis for performing chromophore composition inference using standard least-squares solvers (based on gradient update or pseudoinverse) and our proposed approach. The used spectra for this comparative analysis are taken from the broadband NIRS dataset assuming the scattering model, i.e. they are in the 740nm-900nm range, with a total of 244 measured wavelengths per spectrum, and the underlying chromophores are oxyhemoglobin, deoxyhemoglobin, and differential cytochrome-c-oxidase.

As solving the linear system using the pseudoinverse requires the least amount of matrix multiplication, this method provides the fastest compute. However, with the growth of the number of spectra for which we solve the optimization task, the matrix size for the inversion increases, and thus the computational time increases. Starting from ca. 10^4 amount of spectra, the proposed network having a fixed amount of computational units becomes superior in terms of optimization time. Such runtime will remain approximately constant with a further increasing number of spectra, assuming sufficient GPU memory is available. More importantly, for non-linear systems, which are here represented as a Beer-Lambert model with the inclusion of scattering, one cannot utilize the pseudoinverse and has to resort to non-linear solvers like the ones based on gradient update. Such solvers are two to three orders of magnitude slower than the neural network approach, which has fixed compute time for linear and non-linear systems. As Fig. 14

shows, it takes ca. 0.4 ms for the network to infer biochemical composition for 10^5 spectra on NVIDIA GeForce MX450 with 2048 MiB. Overall, on our hardware, it takes between 2.5 and 3.1 seconds to run the neural network for one an image from the HELICoiD dataset (the largest among all tested data), from opening the normalized HSI image and loading the neural network into the GPU, to displaying the inferred concentrations.

4 Classifying surgical brain tumor biopsy using reconstructed molecular composition

Finally, we present how the spectral unmixing approach described above, based on the modified Beer-Lambert Law, can be used to classify surgical biopsies. The biopsies were collected in the Careggi University Hospital, a partner of the HyperProbe project, from routine glioma patients. In total, we analysed 11 biopsy samples with different grades of tumor classification, high and low grades.

We compare the inferred concentrations for two scenarios: fitting the whole measured wavelength range (from 510nm to 900nm) and fitting only the NIR proportion of the spectrum (in our case, from 740nm to 900nm). For the latter, we expected the major absorbing chromophores to be oxygenated HbO_2 and deoxygenated HHb, the oxidised ($oxCCO$) and reduced ($redCCO$) forms of cytochrome-c-oxidase (CCO), as well as water and lipids. We decided to fit the range between 740nm-780nm (besides the typically used range of 780nm-900nm), as we have shown above that this might be a scattering-dominated band (i.e. allowing to recognize the scattering parameters in our model). Although it is still unknown which chromophores could additionally present major differences in absorbance in the visible light spectrum, we assumed that such additional chromophores might be oxidized and reduced forms of cytochrome-b and cytochrome-c. These possess peaks in the 500nm-600nm range, which we thought to be relevant due to the possible heterogeneity in the metabolic activity of the biopsies. We argue that it is necessary to report results for both scenarios due to the risk of wrongly inferring molecular concentrations, especially in the visible range, as the whole set of absorbing chromophores of tumor biopsies remain unknown.
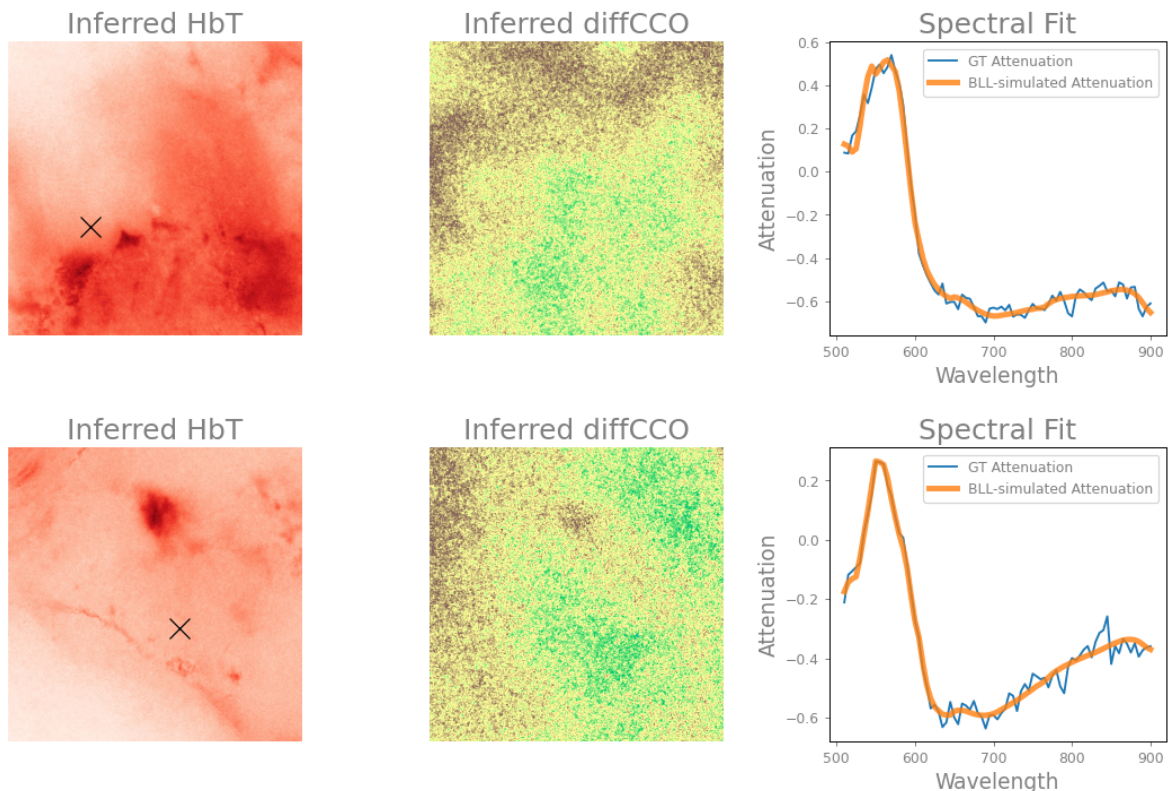
Figure 15: Inferred blood volume (HbT) and differential cytochrome-c-oxidase (diffCCO) concentrations of high grade S4 FOV1 (top) and low grade S10 (bottom) fitting the whole measured wavelength spectrum (510nm-900nm). Model fitting of the observed attenuation for the marked pixel in the HbT image is shown in the third column.

4.1 Results

For the first scenario, we obtain satisfactory spectral fits matching the measured attenuation, as shown in figure 15. Blood clusters are resolved with high resolution, due to the hemoglobin peaks in the 500nm-600nm range and the high expected hemoglobin concentration (compared to other chromophores).

As shown in figure 16, we found lipids to be able to separate low grade (grade II and III) glioma biopsies from high grade glioma biopsies (grade IV) relatively well. Even though we observe significant
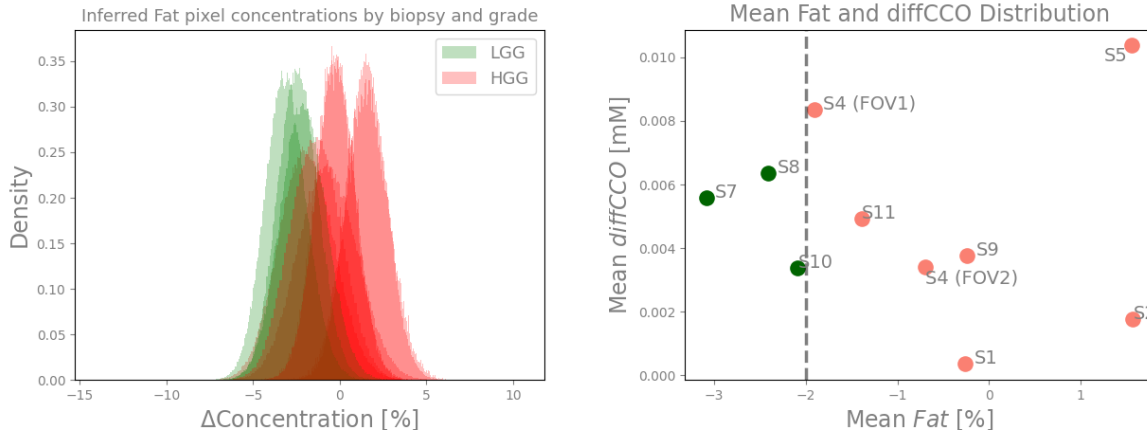
Figure 16: Lipid concentrations can be used to distinguish low and high grade glioma samples when fitting over the entire measured wavelength range. Left: histogram showing density distribution of inferred lipid concentrations of each pixel in low (displayed in green) and high (displayed in red) grade samples. Right: distribution means of lipid (reported on x-axis) and diffCCO (reported on y-axis) show that lipid mean concentrations are able to distinguish all samples, whereas no apparent separation is visible for the inferred mean diffCCO concentrations.

overlap between the different distributions, we generally notice a trend of higher lipid concentrations in high grade biopsies. Substantial lipid storage for lipid metabolism is a known characteristic feature of glioblastoma [31, 49], possibly explaining the difference between lipid content of our low and high grade biopsies. Contrary to our expectations however, we did not find differential cytochrome-c-oxidase (diffCCO) or other molecules to be able to separate the two different grades.

In the second scenario, we report the inferred concentrations using exclusively the NIR range, using chromophores that are known for their characteristic NIRS absorption profile. We are more confident about the inferred concentrations of this scenario, as the BLL has commonly been employed in this range to infer differences in metabolic activity [5]. As shown in figure 17, we again qualitatively fit the observed signal well, albeit being slightly worse due to the expected reduction in SNR at the latter end of the measured spectrum.

Notable loss in the resolution of various blood clusters can be observed, which was also expected due to the exclusion of the 510nm-600nm with large hemoglobin absorption peaks. Interestingly, we observed significant differences to the inferred molecular concentrations. Note that in this scenario, the inferred lipid concentrations were not able to distinguish between the different grades of the samples. However, we noticed metabolic diffCCO differences between low and high grade samples, with high grade samples showing lower diffCCO concentrations, as seen in figure 18.

Oxygenated HbO_2 hemoglobin was additionally found to distinguish most biopsies, which can also be observed in figure 18. Furthermore, we noticed that both oxCCO and redCCO are not able to distinguish biopsy grading. Only the difference between the two inferred concentrations resulted in the shown distinction of the two types. This emphasizes the potential role of differential cytochrome-c-oxidase in providing metabolic differences that lies beyond its critical use in NIRS applications [23]. As the high grade sample 9 additionally displays diffCCO characteristics close to low grade samples, we hypothesized that there could be different (possibly concurrent) reasons for this low distinguishability. Even though it has not been shown that high grade samples can show characteristics of low grade samples, the opposite (i.e. high grade-typical histological characteristics in low grade lesions) has recently been reported [38]. In general, we therefore think that it might be possible that lower grade lesions could display characteristics of higher grade lesions. We highlight two possible mechanistic reasons below.

Firstly, the 2021 World Health Classification between low and high grade gliomas is known to lack metabolic characterisation, instead relying on DNA/RNA chromosomic alterations [33]. We therefore did not expect to be able to separate all low and high grade samples via the inferred diffCCO metabolic
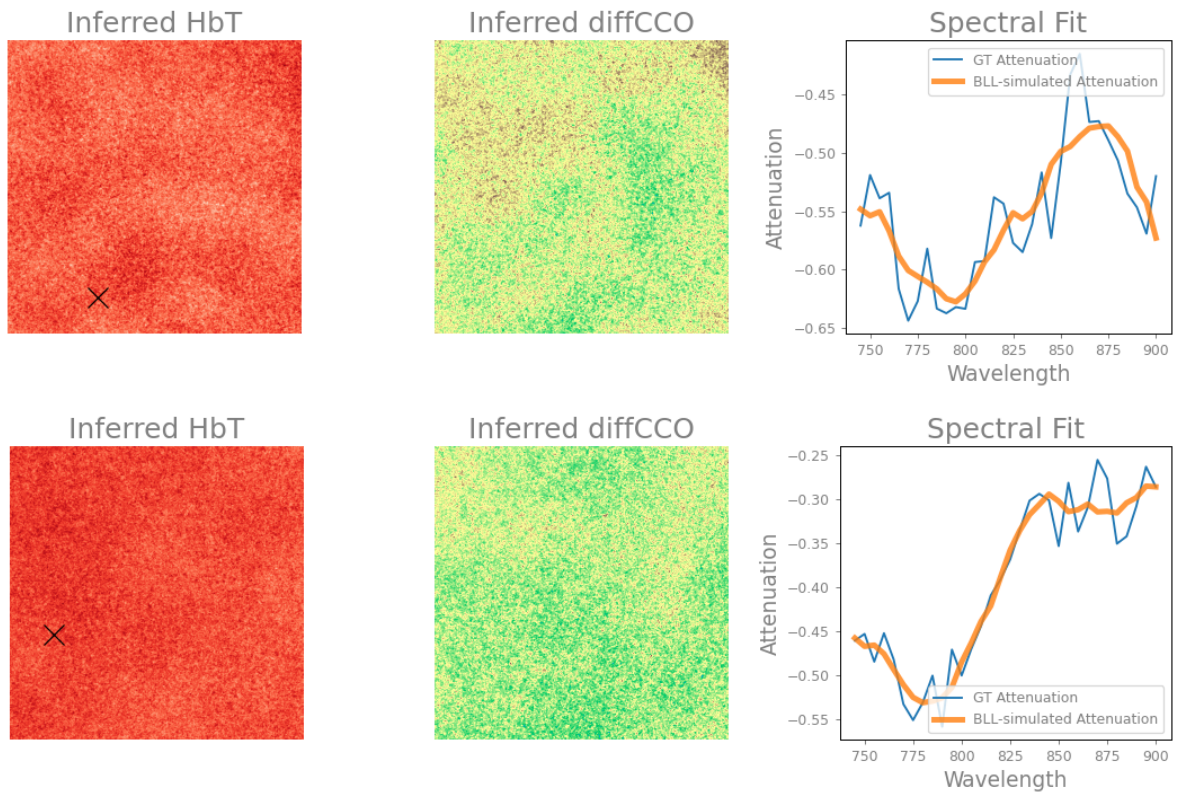
Figure 17: Inferred blood volume (HbT) and differential cytochrome-c-oxidase (diffCCO) concentrations of high grade sample S4 FOV1 (top) and low grade sample S10 (bottom) fitting exclusively the NIR range (740nm-900nm). Model fitting of the observed attenuation for the marked pixel in the HbT image is shown in the third column.

concentrations. Surprisingly, we were still however able to separate most of our samples in the limited set of biopsies. Secondly, we argue that there might be critical immune-mediated differences leading to low distinguishability of S9 [35, 42]. Different infiltration of bone marrow derived macrophages (BMDM) and resident microglia (MG), leading to differences in iron metabolism and immunomodulation of the tumor area, are possible.
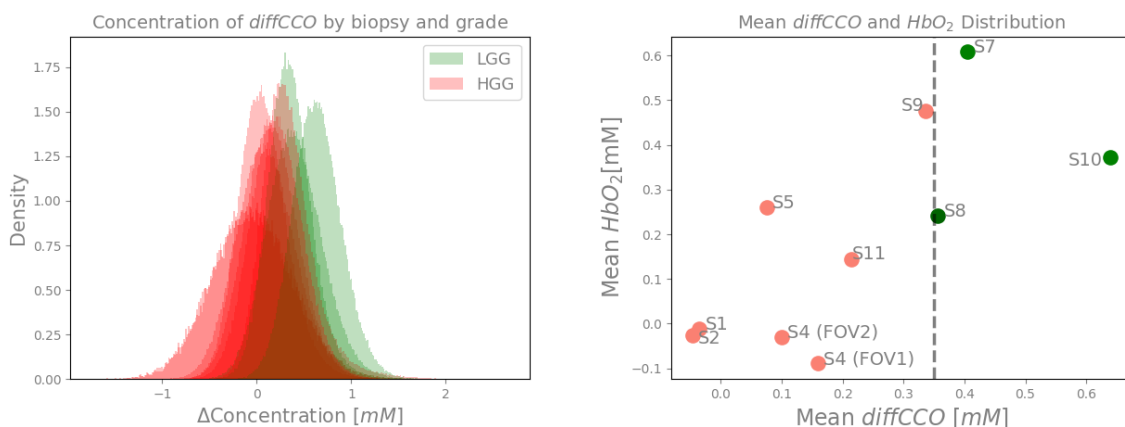
Figure 18: Differential cytochrome-c-oxidase concentrations are able to distinguish low and high grade samples, when fitting exclusively in the NIR range. Left: Histogram showing probability density of inferred diffCCO concentrations of each pixel across different low (displayed in green) and high (displayed in red) grade samples. Right: Distribution means of diffCCO (reported on x-axis) and HbO_2 (reported on y-axis) shows that the inferred distribution means are able to distinguish low and high grade samples.

5 Conclusions

In this report, we present development and validation of algorithmic tools for reconstruction of spectral imaging. We first analyzed HSI glioma images from the HELICoiD project. We performed a PCA-based statistical analysis of this dataset to identify chromophore absorption signatures in the HSI reflection spectra. PCA revealed the correlation of chromophores, especially cytochrome, with the principal components. We discuss the possibility of using such analysis to decypher relative chromophore concentration in brain tissues.

Next, we described a data-driven concept developed for inferring molecular composition change from diffuse spectroscopy of brain tissue. We tested the approach on various datasets (bNIRS and HSI) and physical models of different complexity (with and without scattering, i.e., linear and non-linear systems). Importantly, we evaluated different training strategies for neural-networks-based molecular prediction. The proposed strategy provides predictions that are nearly identical to the traditional least-squares-fit method, making the learnable solver an accurate alternative. The method achieves subsecond time for simultaneous inference of molecular composition across a large number of spectra, allowing for real-time tissue characterization using bNIRS and HSI imaging modalities.

Finally, we analysed the proposed methodology on a surgical biopsy dataset collected within the HyperProbe project. We found significant differences in the inferred concentrations of low and high grade biopsies that allow to distinguish between the two. This observation remains true for both presented inference scenarios with different illumination wavelength range. For the first case the differences arise due to lipid content (having notable peaks in the NIR range), while in the second case they arise especially for diffCCO (also having notable absorption in the NIR range).

The proposed methodology will serve as a basis for image analysis, the focus of the D4.2 deliverable, and be further calibrated on animal and tissue phantom studies carried out within the duration of the HyperProbe project.

Data Repository

The software tools used for all the described works and results have been made publicly available on github under the following link: `https://github.com/HyperProbe/SpectraFit`. The pre-prints of the manuscripts are available on an open-access online archive (arXiv) [14, 15, 26].

References

[1] H. Abramczyk, J. M. Surmacki, B. Brozek-Pluska, and M. Kopec. Revision of commonly accepted warburg mechanism of cancer development: Redox-sensitive mitochondrial cytochromes in breast and brain cancers by raman imaging. *Cancers*, 13(11):2599, 2021.

[2] Y. Altmann, N. Dobigeon, J.-Y. Tourneret, and S. McLaughlin. Nonlinear unmixing of hyperspectral images using radial basis functions and orthogonal least squares. In *2011 IEEE International Geoscience and Remote Sensing Symposium*, pages 1151–1154. IEEE, 2011.

[3] A. Bahl, S. Segaud, Y. Xie, J. Shapey, M. Bergholt, and T. Vercauteren. A comparative study of analytical models of diffuse reflectance in homogeneous biological tissues: Gelatin based phantoms and monte carlo experiments. *arXiv preprint arXiv:2312.12935*, 2023.

[4] G. Bale, C. E. Elwell, and I. Tachtsidis. From jöbsis to the present day: a review of clinical near-infrared spectroscopy measurements of cerebral cytochrome-c-oxidase. *Journal of biomedical optics*, 21(9):091307–091307, 2016.

[5] G. Bale, C. E. Elwell, and I. Tachtsidis. From jöbsis to the present day: a review of clinical near-infrared spectroscopy measurements of cerebral cytochrome-c-oxidase. *Journal of biomedical optics*, 21:091307, Sep 2016.

[6] A. Bateson and B. Curtiss. A method for manual endmember selection and spectral unmixing. *Remote Sensing of Environment*, 55(3):229–243, 1996.

[7] H. Bian, H. Yao, G. Lin, Y. Yu, R. Chen, X. Wang, R. Ji, X. Yang, T. Zhu, and Y. Ju. Multiple kinds of pesticides detection based on back-propagation neural network analysis of fluorescence spectra. *IEEE Photonics Journal*, 12(2):1–9, 2020.

[8] C. Caredda, J. E. Cohen, L. Mahieu-Williame, R. Sablong, M. Sdika, F. C. Schneider, T. Picart, J. Guyotat, and B. Montcel. A priori free spectral unmixing with periodic absorbance changes: application for auto-calibrated intraoperative functional brain mapping. *Biomedical optics express*, 15(1):387–412, 2024.

[9] Y.-W. Chen and S.-H. Tseng. Efficient construction of robust artificial neural networks for accurate determination of superficial sample optical properties. *Biomedical optics express*, 6(3):747–760, 2015.

[10] P.-H. Chou, Y.-H. Yao, R.-X. Zheng, Y.-L. Liou, T.-T. Liu, H.-Y. Lane, A. C. Yang, and S.-C. Wang. Deep neural network to differentiate brain activity between patients with first-episode schizophrenia and healthy individuals: a multi-channel near infrared spectroscopy study. *Frontiers in psychiatry*, 12:655292, 2021.

[11] N. Dobigeon, Y. Altmann, N. Brun, and S. Moussaoui. Linear and nonlinear unmixing in hyperspectral imaging. In *Data Handling in Science and Technology*, volume 30, pages 185–224. Elsevier, 2016.

[12] N. Dobigeon, J.-Y. Tourneret, C. Richard, J. C. M. Bermudez, S. McLaughlin, and A. O. Hero. Nonlinear unmixing of hyperspectral images: Models and algorithms. *IEEE Signal processing magazine*, 31(1):82–94, 2013.

[13] M. Ewerlöf, T. Strömberg, M. Larsson, and E. G. Salerud. Multispectral snapshot imaging of skin microcirculatory hemoglobin oxygen saturation using artificial neural networks trained on in vivo data. *Journal of Biomedical Optics*, 27(3):036004–036004, 2022.

[14] I. Ezhov, L. Giannoni, I. Iliash, F. Hsieh, C. Caredda, F. Lange, I. Tachtsidis, and D. Rueckert. Shallow learning enables real-time inference of molecular composition changes from broadband-near-infrared spectroscopy of brain tissue. *arXiv preprint arXiv:2309.16735*, 2023.

[15] I. Ezhov, L. Giannoni, S. Shit, F. Lange, F. Kofler, B. H. Menze, I. Tachtsidis, and D. Rueckert. Identifying chromophore fingerprints of brain tumor tissue on hyperspectral imaging using principal component analysis. In *European Conference on Biomedical Optics*, 2023.

[16] H. Fabelo, S. Ortega, A. Szolna, D. Bulters, J. F. Piñeiro, S. Kabwama, A. JO'Shanahan, H. Bulstrode, S. Bisshopp, B. R. Kiran, et al. In-vivo hyperspectral human brain image database for brain cancer detection. *IEEE Access*, 7:39098–39116, 2019.

[17] I. Fredriksson, M. Larsson, and T. Strömberg. Machine learning for direct oxygen saturation and hemoglobin concentration assessment using diffuse reflectance spectroscopy. *Journal of Biomedical Optics*, 25(11):112905–112905, 2020.

[18] O. Ganslandt, S. Behari, J. Gralla, R. Fahlbusch, and C. Nimsky. Neuronavigation: concept, techniques and applications. *Neurology India*, 50(3):244, 2002.

[19] I. J. Gerard, M. Kersten-Oertel, J. A. Hall, D. Sirhan, and D. L. Collins. Brain shift in neuronavigation of brain tumors: an updated review of intra-operative ultrasound applications. *Frontiers in Oncology*, 10:618837, 2021.

[20] A. O. Gerstner, W. Laffers, F. Bootz, D. L. Farkas, R. Martin, J. Bendix, and B. Thies. Hyperspectral imaging of mucosal surfaces in patients. *Journal of biophotonics*, 5(3):255–262, 2012.

[21] L. Giannoni and et al. Hyperprobe consortium: innovate tumour neurosurgery with innovative photonic solutions. *ECBO, EB102-52*, 2023.

[22] L. Giannoni, F. Lange, and I. Tachtsidis. Hyperspectral imaging solutions for brain tissue metabolic and hemodynamic monitoring: past, current and future developments. *Journal of Optics*, 20(4):044009, 2018.

[23] L. Giannoni, F. Lange, and I. Tachtsidis. Hyperspectral imaging solutions for brain tissue metabolic and hemodynamic monitoring: past, current and future developments. *Journal of optics (2010)*, 20:044009, Apr 2018.

[24] L. Giannoni, F. Lange, and I. Tachtsidis. Investigation of the quantification of hemoglobin and cytochrome-c-oxidase in the exposed cortex with near-infrared hyperspectral imaging: a simulation study. *Journal of biomedical optics*, 25(4):046001, 2020.

[25] L. Giannoni, M. Marradi, M. Marchetti, D. R. Degl'Innocenti, I. Ezhov, C. Caredda, A. Gautheron, F. Fort, F. Schneider, M. Berhouma, et al. Hyperprobe consortium: innovate tumour neurosurgery with innovative photonic solutions. In *Diffuse Optical Spectroscopy and Imaging IX*, volume 12628, pages 80–87. SPIE, 2023.

[26] L. Giannoni, M. Marradi, K. Scibilia, I. Ezhov, C. Bonaudo, A. Artemiou, A. Toaha, F. Lange, C. Caredda, B. Montcel, et al. A transportable hyperspectral imaging setup based on fast, high-density spectral scanning for in situ quantitative biochemical mapping of fresh tissue biopsies. *arXiv preprint arXiv:2405.20765*, 2024.

[27] B. H. Hokr and J. N. Bixler. Machine learning estimation of tissue optical properties. *Scientific Reports*, 11(1):6561, 2021.

[28] S. L. Jacques. Optical properties of biological tissues: a review. *Physics in Medicine & Biology*, 58(11):R37, 2013.

[29] Y. Karamavuş and M. Özkan. Newborn jaundice determination by reflectance spectroscopy using multiple polynomial regression, neural network, and support vector regression. *Biomedical Signal Processing and Control*, 51:253–263, 2019.

[30] P. Kaynezhad, S. Mitra, G. Bale, C. Bauer, I. Lingam, C. Meehan, A. Avdic-Belltheus, K. A. Martinello, A. Bainbridge, N. J. Robertson, et al. Quantification of the severity of hypoxic-ischemic brain injury in a neonatal preclinical model using measurements of cytochrome-c-oxidase from a miniature broadband-near-infrared spectroscopy system. *Neurophotonics*, 6(4):045009–045009, 2019.

[31] Y. Kou, F. Geng, and D. Guo. Lipid metabolism in glioblastoma: From de novo synthesis to storage. *Biomedicines*, 10, Aug 2022.

[32] R. Liaw, E. Liang, R. Nishihara, P. Moritz, J. E. Gonzalez, and I. Stoica. Tune: A research platform for distributed model selection and training. *arXiv preprint arXiv:1807.05118*, 2018.

[33] D. N. Louis, A. Perry, P. Wesseling, D. J. Brat, I. A. Cree, D. Figarella-Branger, C. Hawkins, H. K. Ng, S. M. Pfister, G. Reifenberger, R. Soffietti, A. von Deimling, and D. W. Ellison. The 2021 who classification of tumors of the central nervous system: a summary. *Neuro-oncology*, 23:1231–1251, Aug 2021.

[34] G. Lu, X. Qin, D. Wang, Z. G. Chen, and B. Fei. Estimation of tissue optical parameters with hyperspectral imaging and spectral unmixing. In *Medical Imaging 2015: Biomedical Applications in Molecular, Structural, and Functional Imaging*, volume 9417, pages 199–205. SPIE, 2015.

[35] S. Magri, B. Musca, L. Pinton, E. Orecchini, M. L. Belladonna, C. Orabona, C. Bonaudo, F. Volpin, P. Ciccarino, V. Baro, A. Della Puppa, and S. Mandruzzato. The immunosuppression pathway of tumor-associated macrophages is controlled by heme oxygenase-1 in glioblastoma patients. *International journal of cancer*, 151:2265–2277, Dec 2022.

[36] M. Mamouei, K. Budidha, N. Baishya, M. Qassem, and P. Kyriacou. An empirical investigation of deviations from the beer–lambert law in optical estimation of lactate. *Scientific Reports*, 11(1):13734, 2021.

[37] T. Manojlović, T. Tomanič, I. Štajduhar, and M. Milanič. Rapid extraction of skin physiological parameters from hyperspectral images using machine learning. *Applied Intelligence*, 53(13):16519–16539, 2023.

[38] K. Motomura, Y. Kibe, F. Ohka, K. Aoki, J. Yamaguchi, and R. Saito. Clinical characteristics and radiological features of glioblastoma, idh-wildtype, grade 4 with histologically lower-grade gliomas. *Brain Tumor Pathology*, 40(2):48–55, 2023.

[39] D. A. Orringer, A. Golby, and F. Jolesz. Neuronavigation in the surgical management of brain tumors: current and future trends. *Expert review of medical devices*, 9(5):491–500, 2012.

[40] I. Oshina and J. Spigulis. Beer–lambert law for optical tissue diagnostics: current state of the art and the main limitations. *Journal of biomedical optics*, 26(10):100901–100901, 2021.

[41] S. Panigrahi and S. Gioux. Machine learning approach for rapid and accurate estimation of optical properties using spatial frequency domain imaging. *Journal of biomedical optics*, 24(7):071606–071606, 2019.

[42] L. Pinton, E. Masetto, M. Vettore, S. Solito, S. Magri, M. D'Andolfi, P. D. Bianco, G. Lollo, J.-P. Benoit, H. Okada, A. Diaz, A. D. Puppa, and S. Mandruzzato. The immune suppressive microenvironment of human gliomas depends on the accumulation of bone marrow-derived macrophages in the center of the lesion. *Journal for ImmunoTherapy of Cancer*, 7(1), 2019.

[43] N. K. Qureshi, F. M. Noori, A. Abdullah, and N. Naseer. Comparison of classification performance for fnirs-bci system. In *2016 2nd International Conference on Robotics and Artificial Intelligence (ICRAI)*, pages 54–57. IEEE, 2016.

[44] D. E. Rumelhart, G. E. Hinton, and R. J. Williams. Learning representations by back-propagating errors. *nature*, 323(6088):533–536, 1986.

[45] A. Scarbrough, K. Chen, and B. Yu. Designing a use-error robust machine learning model for quantitative analysis of diffuse reflectance spectra. *Journal of Biomedical Optics*, 29(1):015001–015001, 2024.

[46] A. A. Stratonnikov and V. B. Loschenov. Evaluation of blood oxygen saturation in vivo from diffuse reflectance spectra. *Journal of biomedical optics*, 6(4):457–467, 2001.

[47] I. Tachtsidis and P. Pinti. UCL NIR spectra. `https://github.com/multimodalspectroscopy/UCL-NIR-Spectra#readme`.

[48] S. Tzoumas and V. Ntziachristos. Spectral unmixing techniques for optoacoustic imaging of tissue pathophysiology. *Philosophical Transactions of the Royal Society A: Mathematical, Physical and Engineering Sciences*, 375(2107):20170262, 2017.

[49] E. Verdugo, I. Puerto, and M. A. Medina. An update on the molecular biology of glioblastoma, with clinical implications and progress in its treatment. *Cancer communications (London, England)*, 42:1083–1111, Nov 2022.

[50] P. Virtanen, R. Gommers, T. E. Oliphant, M. Haberland, T. Reddy, D. Cournapeau, E. Burovski, P. Peterson, W. Weckesser, J. Bright, et al. Scipy 1.0: fundamental algorithms for scientific computing in python. *Nature methods*, 17(3):261–272, 2020.

[51] S. J. Wirkert, H. Kenngott, B. Mayer, P. Mietkowski, M. Wagner, P. Sauer, N. T. Clancy, D. S. Elson, and L. Maier-Hein. Robust near real-time estimation of physiological parameters from megapixel multispectral images with inverse monte carlo and random forest regression. *International journal of computer assisted radiology and surgery*, 11:909–917, 2016.

[52] X. Y. Yap, K. S. Chia, and N. A. S. Suarin. Adaptive artificial neural network in near infrared spectroscopy for standard-free calibration transfer. *Chemometrics and Intelligent Laboratory Systems*, 230:104674, 2022.

[53] K. Yokoyama, M. Watanabe, and E. Okada. Estimation of the optical path length factor for functional imaging of an exposed cortex by principal component analysis. In *European Conference on Biomedical Optics*, page 5138_168. Optica Publishing Group, 2003.

[54] Z. Zhou, L. Zhao, X. Zhang, F. Cui, and L. Guo. Real-time in-situ optical detection of fluid viscosity based on the beer-lambert law and machine learning. *Optics Express*, 30(23):41389–41398, 2022.

[55] W.-X. Zong, J. D. Rabinowitz, and E. White. Mitochondria and cancer. *Molecular cell*, 61(5):667–676, 2016.